New Journal of Physics
The open-access journal for physics

Energy loss spectra of lithium under pressure

A Rodriguez-Prieto[1,2,5,6], **V M Silkin**[1,3], **A Bergara**[1,2,4] **and P M Echenique**[1,3,4]

[1] Donostia International Physics Center (DIPC), Manuel de Lardizabal Pasealekua, E-20018 Donostia, Basque Country, Spain
[2] Materia Kondentsatuaren Fisika Saila, Zientzia eta Teknologia Fakultatea, Euskal Herriko Unibertsitatea, 644 Posta kutxatila, E-48080 Bilbo, Basque Country, Spain
[3] Materialen Fisika Saila, Kimika Fakultatea, Euskal Herriko Unibertsitatea, 1072 Posta kutxatila, E-20080 Donostia, Basque Country, Spain
[4] Centro Mixto CSIC-UPV/EHU, 1072 Posta kutxatila, E-20080 Donostia, Basque Country, Spain
E-mail: alvaro.prieto@ucl.ac.uk

New Journal of Physics **10** (2008) 053035 (18pp)
Received 27 February 2008
Published 29 May 2008
Online at http://www.njp.org/
doi:10.1088/1367-2630/10/5/053035

Abstract. According to the nearly free-electron-like approximation, electrons in alkaline metals are expected to be delocalized under pressure. However, recent theoretical and experimental results strikingly indicate the opposite behavior. For example, under pressure electronic band structure flattens anisotropically and increases the covalent character of alkaline metals, which induces the observed complexities in these systems. Specially considering that even at ambient pressure the observed anomalous features in the loss spectra of lithium cannot be explained within the nearly free-electron-like model, these additional anomalies under pressure are also expected to strongly modify its dynamic electronic response function. In this paper, we present *ab initio* calculations of the energy-loss spectra of lithium up to 40 GPa. Besides analyzing the dispersion of the new type of plasmons arising in lithium under pressure, the role of band structure versus crystal local field effects and exchange correlation has also been investigated.

[5] Present address: London Centre for Nanotechnology (LCN), 17-19 Gordon Street, London, WC1H 0AH, UK.
[6] Author to whom any correspondence should be addressed.

Contents

1. Introduction **2**
2. Theoretical and computational backgrounds **3**
3. Results and discussions **4**
3.1. bcc-Li at equilibrium 4
3.2. fcc-Li at $P = 10$ and 40 GPa 7
4. Conclusions **14**
Acknowledgment **17**
References **17**

1. Introduction

Under normal conditions, free-electron-like approximations are usually enough to describe the main physical properties of alkaline metals. However, it is well known that even at ambient pressure anomalous features observed in the electron energy-loss spectroscopy and inelastic x-ray scattering experiments require to include specific non-free-electron-like characteristics of the band structure, mainly associated with the strong non-local character of the pseudopotential. Among other things, for wavevectors along specific directions, a small additional peak in the loss spectra of lithium [1]–[4] is associated with the so-called zone boundary collective state (ZBCS) [5] and, despite that in most simple metals the width of the main plasmon peak decreases with increasing wavevector momentum in the region of low wavevectors, the opposite behavior has been observed in lithium [6, 7].

Additionally, recent theoretical and experimental high-pressure studies in lithium and other alkalis have revealed a profound change of its bonding and electronic properties. This modification basically relies on the increasing s to p orbital mixing under pressure, which induces a flattening of the electronic band structure and an associated electronic localization [8]–[10]. These modifications strongly distort the Fermi surface of lithium, which shows increasing copper-like necks and extended nestings. This nesting induces a phonon softening which, besides precluding phase transitions to lower coordinated structures [11]–[14] (at normal conditions lithium adopts a compact bcc structure, at around 8 GPa the fcc phase starts to be favored, at 39 GPa a fcc to rhombohedral $hR1$ transition is observed and at 41 GPa the more open $cI16$ phase, with 16 atoms per unit cell, becomes preferred), also enhances the electron–phonon coupling [15]–[19] responsible for the observed increase in the superconducting transition temperature under pressure. Despite lithium having the lowest superconducting transition temperature ($T_c = 0.4$ mK) at normal pressure [20], $T_c = 17$ K when pressure rises to around 30 GPa [21]–[24]. It is remarkable that correlation between low-symmetry phases and the sharp rise of T_c with pressure is not unique to lithium, but has also been observed in other heavier elements [25].

This striking change of electronic properties in compressed lithium is expected to strongly modify its electronic response function. For example, kinks arising in the static electronic susceptibility are correlated with extended nestings in the Fermi surface [12] and a new undamped interband plasmon has been proposed associated with optical interband excitations corresponding to electronic states that drop below the Fermi energy under pressure [26]. In this work, we present an *ab initio* theoretical analysis of the dynamical electronic dielectric

response in lithium for bcc and fcc phases over a wide range of pressures from equilibrium up to 40 GPa and study modifications of the energy loss spectrum, plasmon dispersions and lifetimes under pressure. The paper is organized as follows: section 2 describes the theoretical and computational methods that we have used in this study. In section 3, which is divided into two subsections (bcc-Li and fcc-Li), we present our results. Finally, conclusions are presented in section 4.

2. Theoretical and computational backgrounds

In the linear response theory, the density-response function, $\chi(\mathbf{r}, \mathbf{r}'; \omega)$, of an interacting electron system is defined by the equation

$$n^{\mathrm{ind}}(\mathbf{r}; \omega) = \int \chi(\mathbf{r}, \mathbf{r}'; \omega) V^{\mathrm{ext}}(\mathbf{r}'; \omega)\, \mathrm{d}\mathbf{r}', \tag{1}$$

where $n^{\mathrm{ind}}(\mathbf{r}; \omega)$ is the electron density induced in the system by an external potential $V^{\mathrm{ext}}(\mathbf{r}'; \omega)$. Within the framework of time-dependent density-functional theory (TDDFT) [27, 28], $\chi(\mathbf{r}, \mathbf{r}'; \omega)$ is given by the following integral equation

$$\chi(\mathbf{r}, \mathbf{r}'; \omega) = \chi^0(\mathbf{r}, \mathbf{r}'; \omega) + \int \mathrm{d}\mathbf{r}_1 \int \mathrm{d}\mathbf{r}_2\, \chi^0(\mathbf{r}, \mathbf{r}_1; \omega)\, [V(\mathbf{r}_1 - \mathbf{r}_2) + K_{\mathrm{xc}}(\mathbf{r}_1, \mathbf{r}_2; \omega)] \times \chi(\mathbf{r}_2, \mathbf{r}'; \omega),$$

where $\chi^0(\mathbf{r}, \mathbf{r}'; \omega)$ is the density-response function of the non-interacting electron system, $V(\mathbf{r} - \mathbf{r}')$ is the bare Coulomb interaction and $K_{\mathrm{xc}}(\mathbf{r}, \mathbf{r}'; \omega)$ accounts for the dynamical exchange-correlation effect. In the calculations presented in this paper, we have used both the random-phase approximations (RPAs), where $K_{\mathrm{xc}} = 0$, and time-dependent local-density approximation (TDLDA) [29], where the exchange-correlation kernel is set to

$$K_{\mathrm{xc}}[n_0(\mathbf{r}, \mathbf{r}'; \omega)] = \delta(\mathbf{r} - \mathbf{r}') \left[\frac{\mathrm{d}^2(n\epsilon_{\mathrm{xc}}^{\mathrm{hom}}(n))}{\mathrm{d}n^2} \right]_{n=n_0(\mathbf{r})}, \tag{2}$$

with $\epsilon_{\mathrm{xc}}^{\mathrm{hom}}(n)$ being the exchange-correlation energy per particle of a homogeneous electron gas of density n. For a periodic crystal, the Fourier transform of χ^0 has the following form

$$\chi^0_{\mathbf{G},\mathbf{G}'}(\mathbf{q}, \omega) = \frac{1}{\Omega} \sum_{\mathbf{k}}^{BZ} \sum_{n,n'} \frac{f_{n\mathbf{k}} - f_{n'\mathbf{k}+\mathbf{q}}}{\varepsilon_{n\mathbf{k}} - \varepsilon_{n'\mathbf{k}+\mathbf{q}} + (\omega + \mathrm{i}\eta)} \langle \psi_{n\mathbf{k}} | \mathrm{e}^{-\mathrm{i}(\mathbf{q}+\mathbf{G})\cdot\mathbf{r}} | \psi_{n'\mathbf{k}+\mathbf{q}} \rangle \times \langle \psi_{n'\mathbf{k}+\mathbf{q}} | \mathrm{e}^{\mathrm{i}(\mathbf{q}+\mathbf{G}')\cdot\mathbf{r}} | \psi_{n\mathbf{k}} \rangle.$$

Here $\mathbf{G}$, $\mathbf{G}'$ are the reciprocal lattice vectors, the wavevectors $\mathbf{k}$ and $\mathbf{q}$ are in the first Brillouin zone (BZ), $f_{n\mathbf{k}}$ represents the Fermi–Dirac distribution function, η is a positive infinitesimal, and Ω is the normalization volume. The one-electron energies, $\varepsilon_{n,\mathbf{k}}$, and wavefunctions, $\psi_{n,\mathbf{k}}$, represent the self-consistent electronic structure calculated within the local-density approximation (LDA) to the density-functional theory (DFT) with the electron–ion interaction of lithium described by a norm-conserving pseudopotential [30]. In the expansion of χ^0 and χ, 20 reciprocal vectors $\mathbf{G}$ were included. Therefore, crystal local field effects are included through the inversion of the matrix representation of equation (2). The first summation in equation (3) was performed with the use of a $144 \times 144 \times 144$ ($96 \times 96 \times 96$) $\mathbf{k}$-mesh for the bcc (fcc) lattice, which corresponds to 746 496 (442 368) points in the BZ. The second sum

runs over the occupied and all unoccupied valence bands up to an energy of 50 eV above the Fermi level. We avoid the direct evaluation of χ^0 using equation (3) by calculating at the first step the spectral-function matrix $S^0_{\mathbf{G},\mathbf{G}'}(\mathbf{q},\omega)$, from which the imaginary parts of the $\chi^0_{\mathbf{G},\mathbf{G}'}(\mathbf{q},\omega)$ matrices are readily obtained [31]. Subsequently, the real part of χ^0 is obtained from the $\mathrm{Im}\chi^0$ through the Kramers–Kronig relations. Numerically, in the evaluation of $S^0_{\mathbf{G},\mathbf{G}'}(\mathbf{q},\omega)$ the δ-function was replaced by a Gaussian $(\sqrt{\pi}\sigma)^{-1}\exp(-\omega^2/\sigma^2)$ with $\sigma = 0.1$ eV [32]. The energy-loss spectrum $S(\mathbf{q},\omega)$ is given by the imaginary part of the inverse macroscopic dielectric function $S(\mathbf{q},\omega) = -\mathrm{Im}[\epsilon^{-1}(\mathbf{q},\omega)]$, where $\epsilon^{-1}(\mathbf{q},\omega)$ is the Fourier transform of $\epsilon^{-1}(\mathbf{r},\mathbf{r}',\omega)$ and is defined as $\epsilon^{-1} = 1 + V\chi$ in the abbreviated form. In ideal conditions, the frequency of the plasmon is given by the frequency at which both the real and the imaginary parts of $\epsilon(\mathbf{q},\omega)$ are zero. However, as the plasmon is usually damped by the electron–hole (e–h) mechanism, we define the plasmon frequency to be the positions of the main peaks in the energy-loss spectrum.

Effects of compression have been simulated by reducing the lattice parameter. For bcc-Li at equilibrium, we use the calculated lattice parameter of $a = 3.515$ Å. For fcc-Li at $P = 10$ and 40 GPa, the lattice parameters are $a = 3.74$ and 3.32 Å, respectively.

3. Results and discussions

3.1. bcc-Li at equilibrium

Figure 1 shows the calculated energy loss spectra, $-\mathrm{Im}[\epsilon^{-1}]$, of bcc-Li at $P = 0$ along three different high-symmetric directions: ΓH, ΓN and ΓP (or [100], [110] and [111], respectively). Plasmons are clearly visible by maximum values of the energy loss spectra. Despite the clear anisotropy observed, bcc-Li shows two main collective modes at $P = 0$: the conventional free-electron-like plasmon, labeled as 'A' in the figure, and also another kind of collective mode, labeled as 'B', which has been associated with the so-called ZBCS. The main peak 'A' is centered at around 7.25 eV at very small momentum transfers, $|\mathbf{q}| \sim 0$, and appears along all symmetry directions. The ZBCS has been previously reported to emerge only along the [110]-direction for momentum transfers larger than 0.4 Å^{-1} [7]. However, our calculations show this ZBCS to arise also in the finite small momentum region, along the three directions considered. We attribute these differences to the more dense **k** mesh we have implemented in our calculations, which permits the resolution of much finer details. For instance, Jin and Ghang [7] make use of the N-point Padé approximant with around 81 irreducible **k**-points and a damping parameter of 0.5 eV. In our calculations, we avoid the use of the N-point Padé approximant and increase the number of irreducible **k**-points from 81 to ∼15 000.

However, the ZBCS gets strongly damped due to a coupling to e–h excitations, as we can see in figure 2, where we plot the damping function, $-\omega \cdot \mathrm{Im}[\epsilon]$, of bcc-Li at equilibrium. Here, we also display by solid red lines the plasmon dispersions extracted from figure 1. In figure 2, one can see how for higher values of the momentum transfers along the [100] and [111]-directions, the ZBCS gets completely damped due to a coupling to e–h excitations and, hence, disappears. Nevertheless, the special shape of the e–h excitation continuum along [110]-directions in the low-energy region leads to the existence of the ZBCS also in the higher momentum region, at an energy of ∼4.5 eV, approximately 1 eV higher than in the small momentum region. It is also noteworthy that the ZBCS does not exist for very small momenta, $|\mathbf{q}| < 0.2$ Å^{-1}, along any of the three directions considered. The shape of the e–h excitation spectrum is associated with the almost planar geometry of the two lowest energy bands around

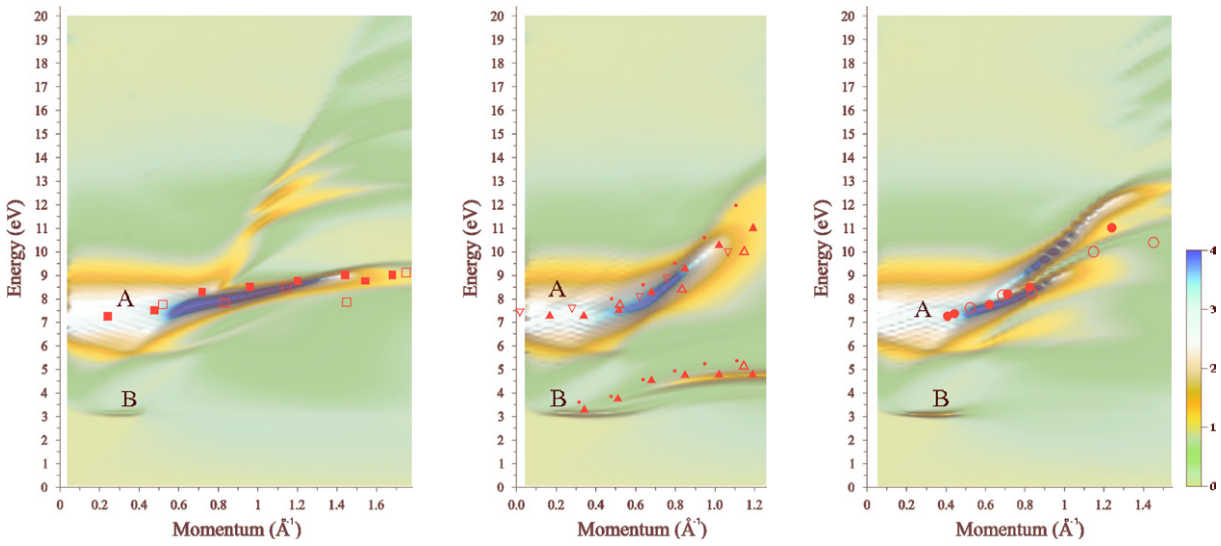

Figure 1. Energy-loss spectra, $-\mathrm{Im}[\epsilon^{-1}]$, of bcc-Li at equilibrium along the three momentum symmetry directions: [100] (left panel), [110] (center panel) and [111] (right panel). The crystal local field effects (CLFE) (via inversion of the full dielectric matrix), as well as exchange-correlations (via inclusion of the TDLDA kernel) are included. Color code is explained in the right bottom part of the figure. The dominant plasmon peak is denoted by 'A'. Please note the appearance of the ZBCS (feature 'B') along all three momentum directions and not only along the [110]-direction, as proposed previously. Calculated results of [7] are shown by full squares, triangles and circles and of [6] by dots. Empty squares, triangles and circles show experimental data [2, 3]. Inverse empty triangles are experimental data of [1].

the N point of the BZ. The threshold for the transitions between these two bands is highlighted by a vertical red arrow in figure 3 and it is precisely the presence of this kind of transition between occupied p states and unoccupied s states around the N point, which leads to the appearance of the ZBCS.

In figure 4, we present the plasmon width (the width of the plasmon peak at half maximum height) along both the [100]- and [110]-directions. In spite of the opposite being observed for other simple metals [6, 7], the 'A' plasmon width decreases with increasing momentum transfer. Again, the width dispersion depends on the direction. On the one hand, along the [110]-direction, and due to an absorption power redistribution, for $\mathbf{q}$ greater than 0.7 Å^{-1} the 'A' plasmon width starts to increase and, hence, the lifetime is reduced. On the other hand, along the [100]-direction the ZBCS is scattered by e–h excitations at lower momenta, $\mathbf{q} \sim 0.67$ Å^{-1}, whereas the 'A' plasmon does not enter the e–h excitation continuum (see figure 2) and, hence, remains well defined for higher wavevectors. It is noteworthy that in spite of the ZBCS width dispersion staying very flat along the [110]-direction, an energy shift of ∼0.26 eV can be observed at $\mathbf{q} \sim 0.67$ Å^{-1}.

In order to check the role of both CLFE and exchange-correlation on the energy loss function of bcc-Li at equilibrium, we have calculated the dielectric function (real and imaginary parts) and its corresponding loss function at two selected values of the momentum transfer

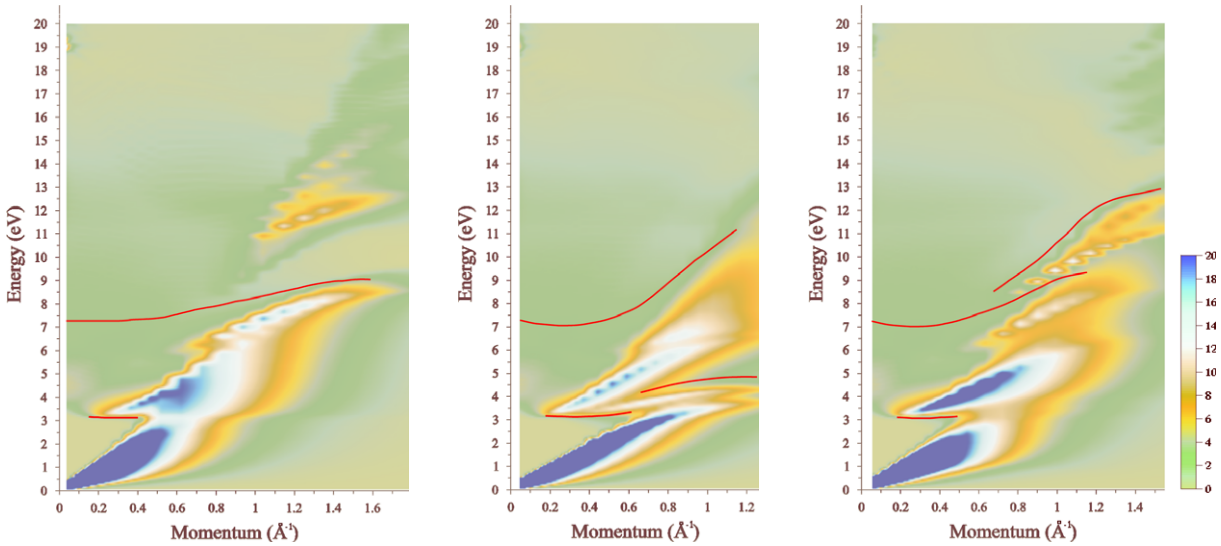

Figure 2. Damping function, $-\omega \mathrm{Im}[\epsilon]$, of bcc-Li at equilibrium along the three symmetric momentum directions: [100] (left panel), [110] (center panel) and [111] (right panel). Plasmon dispersions from figure 1 are shown by solid red lines. CLFE (via full inversion of the dielectric matrix), as well as exchange and correlation effects (via inclusion of the TDLDA kernel) are included. Color code is the same as in figure 1.

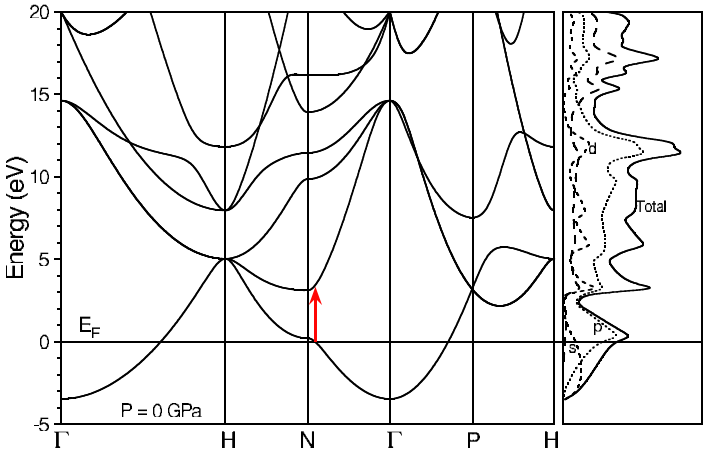

Figure 3. Energy band structure along some symmetry directions of the BZ (left panel) and density of states (DOS) (right panel) of bcc-Li at equilibrium. The red arrow shows the threshold for inter-band optical transitions that lead to the appearance of the ZBCS. The partial contributions to the total DOS from states of s, p and d symmetries are denoted by corresponding symbols.

along the [100]-direction, $\mathbf{q} = 0.364\,\text{Å}^{-1}$ (figure 5) and $\mathbf{q} = 1.039\,\text{Å}^{-1}$ (figure 6), within both the RPA and TDLDA. We can observe that at small momentum transfers similar results are obtained within both the RPA and TDLDA calculations, with and without including the CLFE. Nevertheless, when the momentum transfer is increased, the influence of the CLFE starts to be

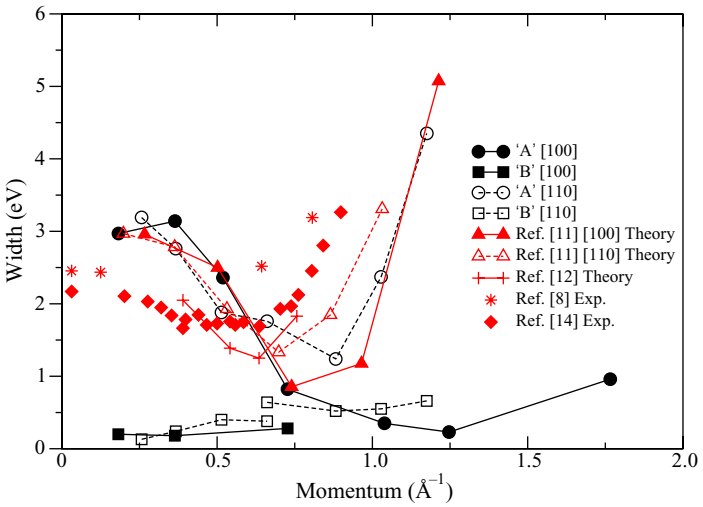

Figure 4. Plasmon widths versus momentum in bcc-Li at equilibrium. Full (open) circles connected by a solid (dashed) line represent 'A' width along the [100] ([110])-direction. On the other hand, full (open) squares connected by a solid (dashed) line represent 'B' width along the [100] ([110])-direction. All our theoretical calculations are plotted in black. In order to compare with other results, we display in red the previous theoretical and experimental data: full (open) up triangles connected by a solid (dashed) line represent plasmon width along the [100] ([110])-direction as theoretically calculated in [7], the theoretical results of [6] are shown by pluses connected by a solid line, whereas experimental data reported in [1, 33] are plotted by stars and full diamonds, respectively.

significant. However, this influence is quantitative but not qualitative, in the sense that CLFE do not fundamentally modify the main features of the loss function: our spectra, either one takes or does not take CLFE into account, consists of two collective modes (one associated with a ZBCS, the other being a free-electron-like plasmon), and the only effect of the CLFE is to modify the height of these peaks when a high momentum transfer is considered.

The differences, in the high-momentum transfer region, between the RPA and TDLDA approximations are: the loss function which includes the CLFE gets enhanced within the TDLDA approximation, whereas that loss function which does not include the CLFE remains similar within both the approximations. A similar effect of the CLFE and exchange-correlation on plasmon properties is observed also for fcc-Li at different pressures.

In the following subsection, we consider fcc-Li under pressures ranging from 10 GPa up to 40 GPa. In this way, we are able to study the pressure-induced modifications in the dielectric and energy loss functions of lithium.

3.2. fcc-Li at $P = 10$ and 40 GPa

We first start analyzing fcc-Li at $P = 10$ GPa, close to the bcc $\rightarrow$ fcc structural phase transition. Figure 7 displays the calculated low-momentum dielectric function, $\epsilon(\mathbf{q} \rightarrow 0, \omega)$, together with its corresponding energy loss spectrum. Note that both the CLFE (via full inversion of the

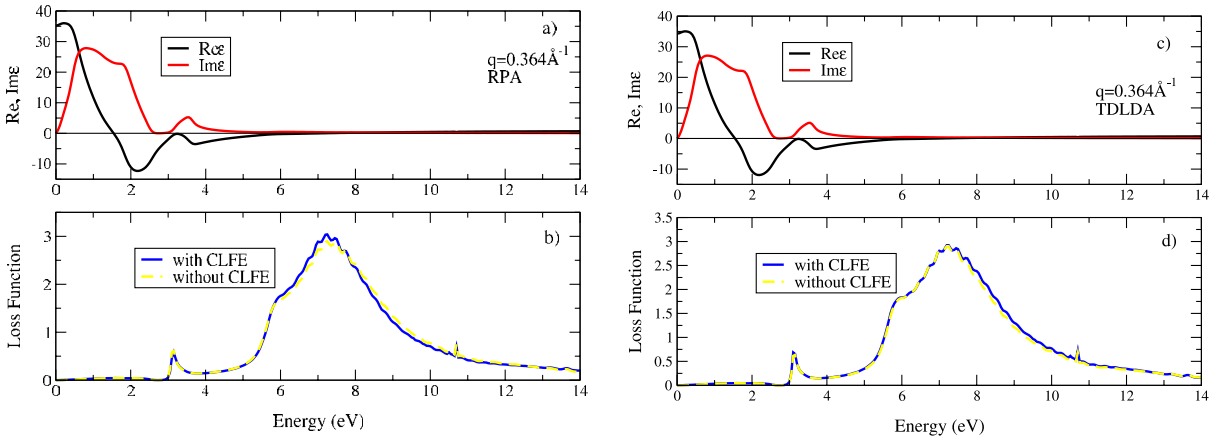

Figure 5. Role of CLFE and exchange-correlations on the dielectric and loss functions of bcc-Li at equilibrium at $q = 0.364\,\text{Å}^{-1}$ along the [100]-axis. Top panels (a) and (c) present the calculated imaginary (red lines) and real (black lines) parts of the dielectric function. In bottom panels (b) and (d) energy-loss functions with (without) taking into account the CLFE are shown by blue solid (yellow dashed) lines. Left (right) column of the figure corresponds to the RPA (TDLDA) model.

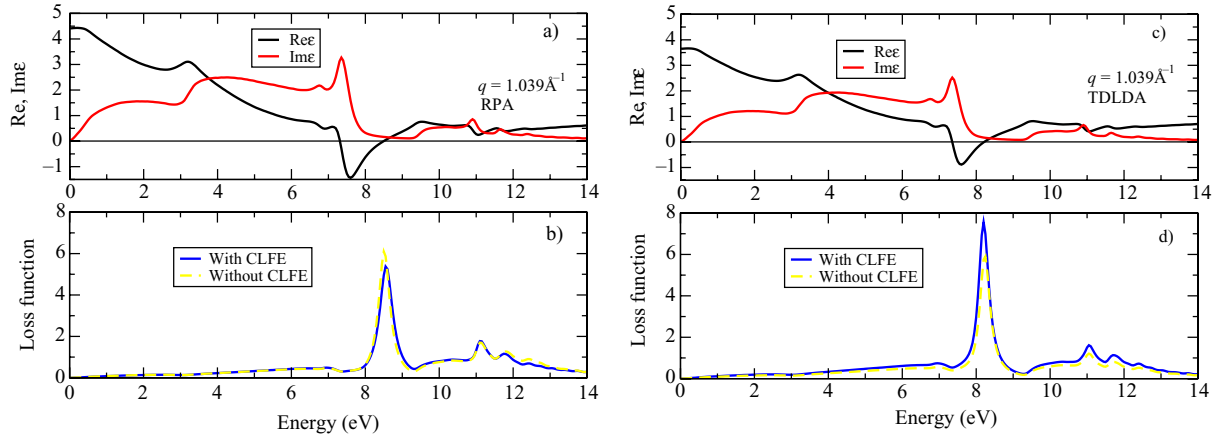

Figure 6. Role of CLFE and exchange-correlations on the dielectric and loss functions of bcc-Li at equilibrium at $q = 1.039\,\text{Å}^{-1}$ along the [100]-axis. Top panels (a) and (c) present calculated imaginary (red lines) and real (black lines) parts of the dielectric function. In bottom panels (b) and (d) energy-loss functions with (without) taking into account the local-field effects are shown by blue solid (yellow dashed) lines. Left (right) column of the figure corresponds to the RPA (TDLDA) model.

matrix) and exchange-correlation (via TDLDA approximation) are taken into account for all the calculations presented for fcc-Li. It is known that under pressure, and contrary to the case of bcc-Li at equilibrium, the electronic band structure of fcc-Li is not free-electron-like anymore. Therefore, as the emergence of the ZBCS for bcc-Li at equilibrium was a direct consequence

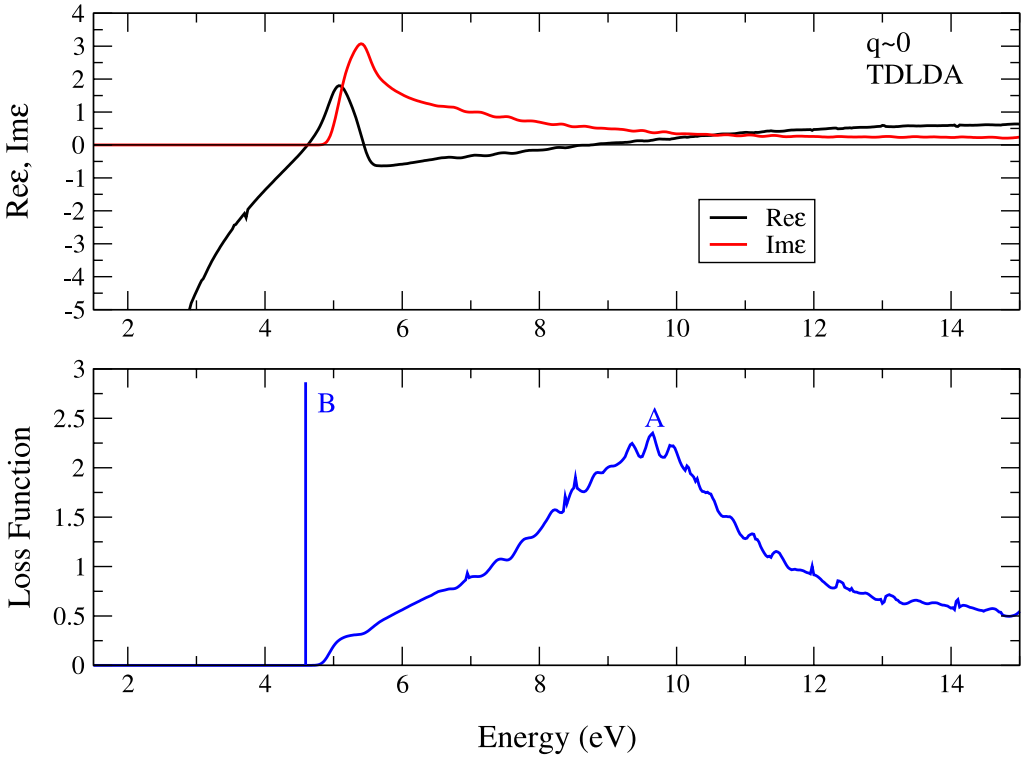

Figure 7. Top panel: low-momentum dielectric function of fcc-Li at $P = 10$ GPa. Re[ϵ] and Im[ϵ] are plotted by black and red lines, respectively. Bottom panel: corresponding energy-loss function with CLFE included. It is remarkable that at $\omega = 4.7$ eV the dielectric function vanishes, $\epsilon = 0$, which produces a δ-function-like peak in the energy-loss function at the same energy.

of the so-called band structure effects, we can expect them to be more important at $P = 10$ GPa than at equilibrium. As one can observe in figure 7, Re[ϵ] goes to zero at three different energies in the 4–9 eV energy range, which leads to the appearance of two collective modes. That one labeled by 'A' in the figure corresponds to the conventional free-electron-like plasmon, which is determined by the average valence electronic density. 'A' plasmon presents a wide peak at $\sim$9 eV with a width of 2.3 eV, and is similar to that plasmon observed earlier for bcc-Li at equilibrium (also labeled by 'A' in figures 1 and 2). Interestingly, another peak in the loss function (labeled by 'B') arises at 4.7 eV, which becomes remarkable different. Both the real and imaginary parts of the dielectric function vanish, Re[ϵ] = Im[ϵ] = 0, which fulfills the ideal condition for the existence of a well-defined undamped plasmon. Therefore, this plasmon is not scattered due to any e–h excitations. As a consequence, it presents an infinite lifetime, which is reflected in the δ-peak shown by the loss function at 4.7 eV.

The physical origin of this striking feature is associated with the sharp increase of Im[ϵ] at $E_0 = 5.1$ eV, which corresponds to the threshold energy for the optical ($\mathbf{q} \to 0$) interband transitions around the L point, shown by red arrows in figure 8, connecting electronic states with $\Delta l = 1$, as required for optical transitions. Pressure-induced anisotropic flattening of bands drops electronic states near the L point below the Fermi energy and it is precisely the presence of almost flat regions in both occupied (mainly of p symmetry) and unoccupied (mainly of

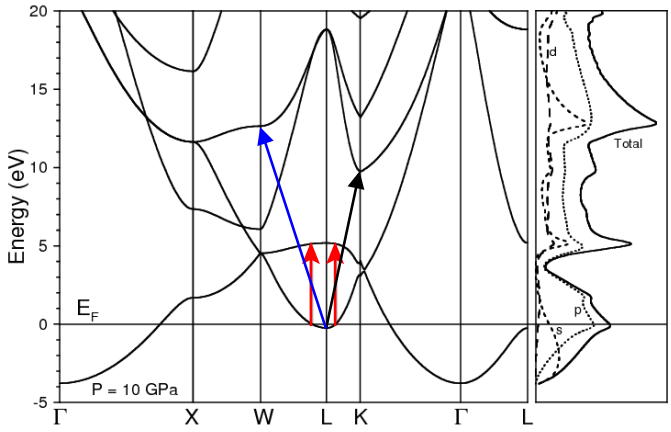

Figure 8. Energy band structure along some symmetry directions of the BZ (left panel) and DOS (right part) of fcc-Li at $P = 10$ GPa. The partial contributions to the total DOS from states of s, p and d symmetries are denoted by corresponding symbols. The thresholds for the L–L, L–W and L–K inter-band transitions are represented with red, blue and black arrows, respectively.

s symmetry) states around the L point which leads to the observed steep increase in Im[ϵ] at E_0. Thus, we can conclude that the important band structure effects in lithium under pressure lead to the appearance of a novel feature: an undamped plasmon.

Figure 9 shows the loss function of fcc-Li at $P = 10$ GPa along the three symmetric directions: [100], [110] and [111], whereas figure 10 displays the damping function, $-\omega$ Imϵ, of fcc-Li at $P = 10$ GPa along the same directions. We can observe that in the low-momentum region the loss function spectra consist mainly of two collective charge excitations, 'A' and 'B'. Actually, the 'B' feature presents a δ-function-like peak (as happened for $|\mathbf{q}| \to 0$) in this region because, when low momentum dispersion of this novel feature is considered, the almost planar geometry of energy bands around the L point makes it undamped in any direction (see figure 10). However, for higher momentum transfers, $|\mathbf{q}| > 0.7\,\text{Å}^{-1}$ along the [100] and [110]-directions and $|\mathbf{q}| > 1.1\,\text{Å}^{-1}$ along the [111]-direction, the 'B' feature starts to get scattered by the e–h one-particle mechanism and, thus, tends to disappear.

It is also remarkable that the ZBCS appearing at lower momenta in bcc-Li can be considered as a predecessor of this novel undamped plasmon in the fcc lattice under pressure. In bcc-Li at $P = 0$, inter-band transitions around the N point of the BZ (the lowest energy band is not occupied in close vicinity to N) between occupied p-symmetry and unoccupied s-symmetry states constituted the physical origin of the ZBSC. Let us recall also that a finite momentum is needed in order to excite the ZBCS in bcc-Li at equilibrium. With the application of a pressure of 10 GPa to the bcc phase, one can observe how, like the case of fcc, the applied pressure drops electronic states near the N point below the Fermi energy. Thus, the whole lowest electronic band along ΓN becomes occupied. This drop increases the number of possible N–N inter-band transitions (similarly to the L–L in the fcc-Li) with energy 5.5 eV (energy gap at the N point) and, therefore, enhances the original ZBCS, which becomes a well-defined undamped plasmon and is already excited at $\mathbf{q} = 0$, where the energy-loss function exhibits a δ-peak and both the real and imaginary parts of the dielectric functions vanish.

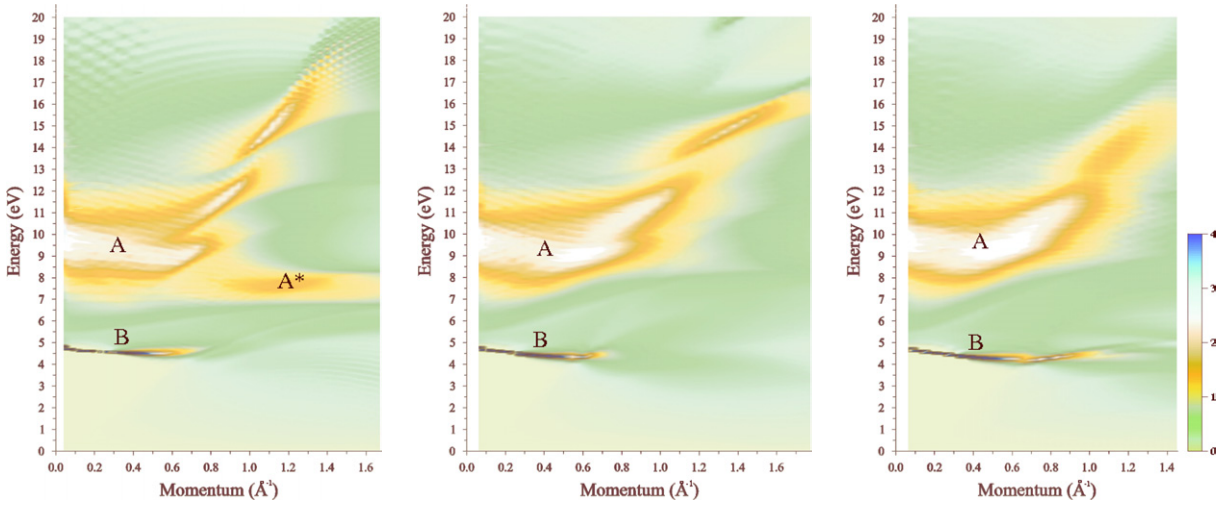

Figure 9. Energy-loss spectra, $-\mathrm{Im}[\epsilon^{-1}]$, of fcc-Li at $P = 10$ GPa along the three symmetry momentum directions; [100] (left panel), [110] (center panel) and [111] (right panel). The CLFE (via inversion of the full dielectric matrix), as well as exchange-correlations effects (via inclusion of the TDLDA kernel) are included. Color code is explained in the right bottom part of the figure. The 'A' plasmon shows a parabolic-type dispersion and its energy increases significantly in comparison with the corresponding 'A' mode in bcc-Li. In addition, new inter-band collective excitations give rise to two unfoldings of the 'A' plasmon. Another fundamental difference between bcc-Li at equilibrium and fcc-Li at 10 GPa is that in the latter case the 'B' plasmon already becomes excited at $\mathbf{q} = 0$ and extends over a wider momentum transfer region.

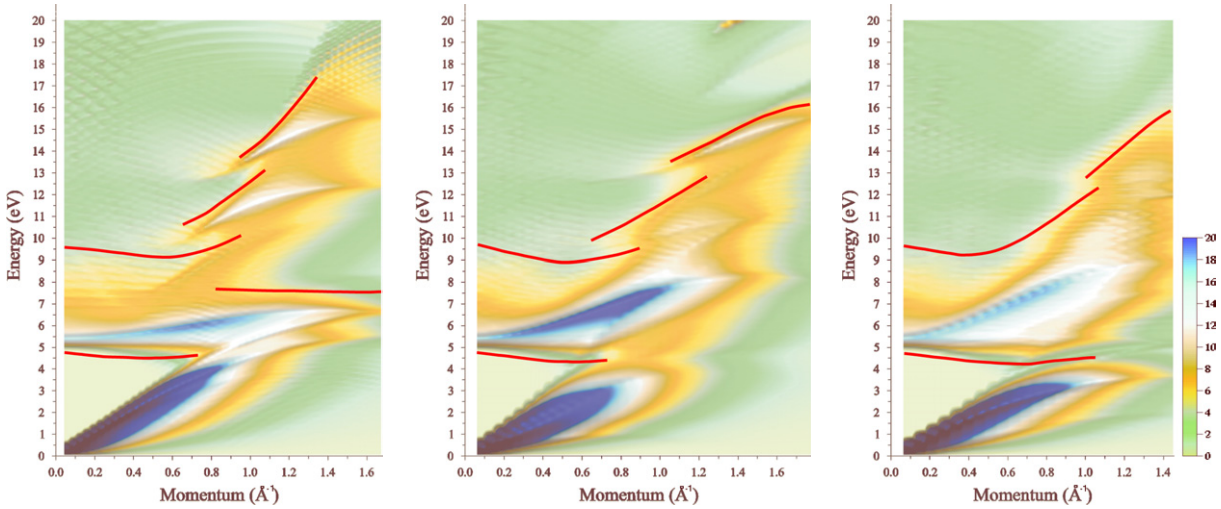

Figure 10. Damping function, $\omega \cdot \mathrm{Im}[\epsilon]$, of fcc-Li at $P = 10$ GPa along the three symmetry momentum directions: [100] (left panel), [110] (center panel) and [111] (right panel). Plasmon dispersions in figure 9 are shown by solid red lines. Color code is explained in the right bottom part of the figure.

Even more, the energy bands in bcc-Li at 10 GPa exhibit flat regions around the N point, again similar to the L point in the case of fcc-Li, which makes the 'B' plasmon undamped in any momentum direction.

Regarding the 'A' collective mode, and contrary to the case of bcc-Li at equilibrium, it is fundamentally affected by the band structure effects, which have been enhanced due to the pressure-induced electronic localization (reflected in the flattening of the electronic bands). These band structure effects are specially visible along the [100]-direction, where we observe a quite complex structure for the 'A' plasmon at higher momenta. When the momentum transfer is increased, at around $|\mathbf{q}| = 0.8\,\text{Å}^{-1}$, the e–h excitations become enhanced. The energy of these one-particle excitations reaches the inter-band L–L transitions and produces a rapid decrease in Im[ϵ] which leads to the appearance of a shoulder structure labeled as 'A*' in the left panel of figure 9. This shoulder structure does not appear along either the [110]- or [111]-direction, because the e–h excitation continuum presents a larger width along these two directions and, hence, 'A*' gets completely scattered by one-particle excitations and disappears. Apart from this feature, 'A' exhibits similar behavior along the three directions considered, with a slightly negative dispersion at low momenta. At $|\mathbf{q}| = 0.7\,\text{Å}^{-1}$, a first unfolding of the plasmon is produced, with a shift in energy from 9.5 to 10.5 eV. The physical origin of this first unfolding resides in the inter-band excitations between the occupied states around the L point (mainly of p-symmetry) and the unoccupied states around the K point (mainly of s-symmetry). These inter-band L–K transitions are plotted with blue arrows in figure 8. The 'A' plasmon shows a positive dispersion for momentum transfers $|\mathbf{q}| > 0.7\,\text{Å}^{-1}$, and close to $|\mathbf{q}| = 1\,\text{Å}^{-1}$ suffers a second unfolding, mainly due to the inter-band excitations between p-occupied states around the L point and d-unoccupied states around the W point, with an energy of 14 eV. These interband L–W transitions are represented by black arrows in figure 8. One can see that, as a consequence of the pressure-induced band flattening (which indicates that lithium deviates from the free-electron-like model under pressure), the band structure effects become strong enough to make the 'A' collective charge excitation depart from a conventional free-electron-like plasmon at higher momentum transfers.

In addition, the width dispersion of both collective charge excitations 'A' and 'B' for fcc-Li at 10 GPa are displayed in figure 11. We just consider wavevectors up to $0.9\,\text{Å}^{-1}$ as for greater momenta the 'A' plasmon structure suffers several unfoldings and its corresponding energy-loss function is divided into several wide peaks, where it is difficult to fix a criterion in order to analyze its width. Some of these peaks do not even correspond to zeros in the real part of the dielectric function. Despite the dielectric function presenting some clear minima, it does not vanish, which complicates even more the ascriptions of these peaks. In addition, for large $|\mathbf{q}|$ values the plasmon 'B' gets strongly coupled to e–h excitations. However, this collective charge excitation is completely undamped in the low momentum region, $|\mathbf{q}| < 0.3\,\text{Å}^{-1}$, presenting a zero width. At higher momenta, its width starts to increase reaching a maximum value of 0.8 eV at $0.7\,\text{Å}^{-1}$, which constitutes a prelude to its extinction as it becomes highly coupled to particle–hole excitations. On the other hand, the 'A' plasmon presents a small increase of its width in the very low momenta region, reaching a maximum value of 3.97 eV at $0.27\,\text{Å}^{-1}$ along [100] and 4.17 eV at $0.33\,\text{Å}^{-1}$ along [110], before starting to decrease.

In order to analyze the evolution of both plasmons under pressure, we have also performed similar calculations at $P = 20$, 30 and 40 GPa. Figure 12 displays the calculated energy-loss function (top line panels) together with the imaginary part of the dielectric function and the plasmon dispersion (bottom line panels) of fcc-Li along the highly symmetric directions ΓX,

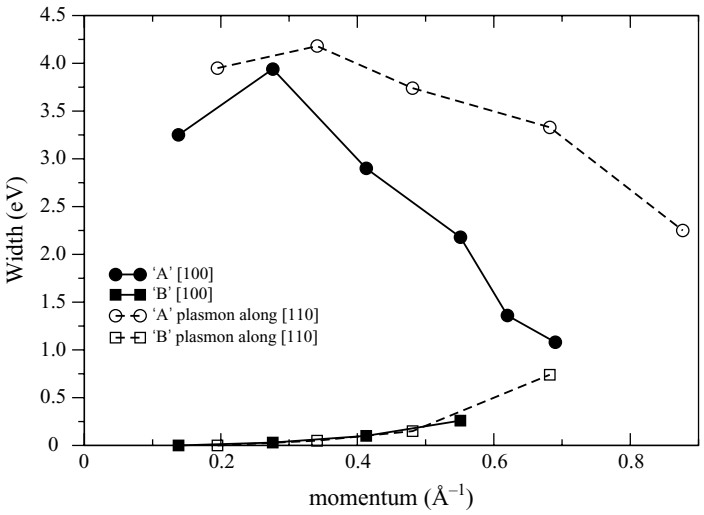

Figure 11. Plasmon width versus momentum for fcc-Li at $P = 10$ GPa. Full (open) circles connected by a solid (dashed) line represent 'A' width along the [100] ([110])-direction. On the other hand, full (open) squares connected by a solid (dashed) line represent 'B' width along the [100] ([110])-direction.

ΓK and ΓL, at 40 GPa, just before the fcc $\rightarrow hR1$ phase transition takes place. For clarity, in figure 13 we have also plotted the dielectric function and corresponding energy-loss spectra at $\mathbf{q} = 0$. Effects of pressure can be clearly deduced from comparison of figures 7 and 13. It is easy to conclude that the inter-band transition threshold E_0, i.e. the energy at which a sharp increase of Im[ϵ] is produced, gradually increases with pressure (from $E_0 = 5.1$ eV at 10 GPa to $E_0 = 7.5$ eV at 40 GPa), as a consequence of the growing energy-gap around the L point (see figure 14). This increasing energy-gap requires more energy in order to excite the optical inter-band transitions and induces a blueshift of the main peak in Im[ϵ], which increases the energy corresponding to the 'B' plasmon. On the other hand, the increasing of the total valence electron density also leads to increasing energy of the 'A' plasmon. Another interesting feature is that we can observe a clear absorption power redistribution from the free-electron-like plasmon 'A' to the undamped 'B' plasmon. This is also a direct consequence of the electronic band structure under increasing pressure, which is even flatter and less free-electron-like at $P = 40$ GPa and whose gap at the L point is significantly larger.

Figure 15 displays the plasmons width at 40 GPa along the [100]- and [110]-directions. Comparing it to figure 11, one can note that the 'B' plasmon remains undamped at higher momentum transfers, which is a consequence of the opening of a gap in the e–h excitation region which allows the 'B' plasmon not to get coupled to one-particle excitations at higher values of $\mathbf{q}$. On the other hand, the opposite is observed for the 'A' plasmon whose coupling to one-particle excitations is stronger than at 10 GPa.

Finally, the existence of the 'B' plasmon leads to a dramatic modification of the optical properties of lithium under pressure [26]. When the frequency of the incident light is slightly above the 'B' plasmon frequency, it would experience an abrupt decrease in reflectivity with the subsequent total loss of reflectivity at $\sim$5 eV ($\sim$7 eV) for $P = 10$ GPa ($P = 40$ GPa). Calculations of the optical constants at 20 and 30 GPa give similar results, with vanishing reflectivity around 5.9 and 6.5 eV, respectively. On the other hand, it is also remarkable that the reflectivity of fcc-Li is fundamentally different from that of bcc-Li [26].

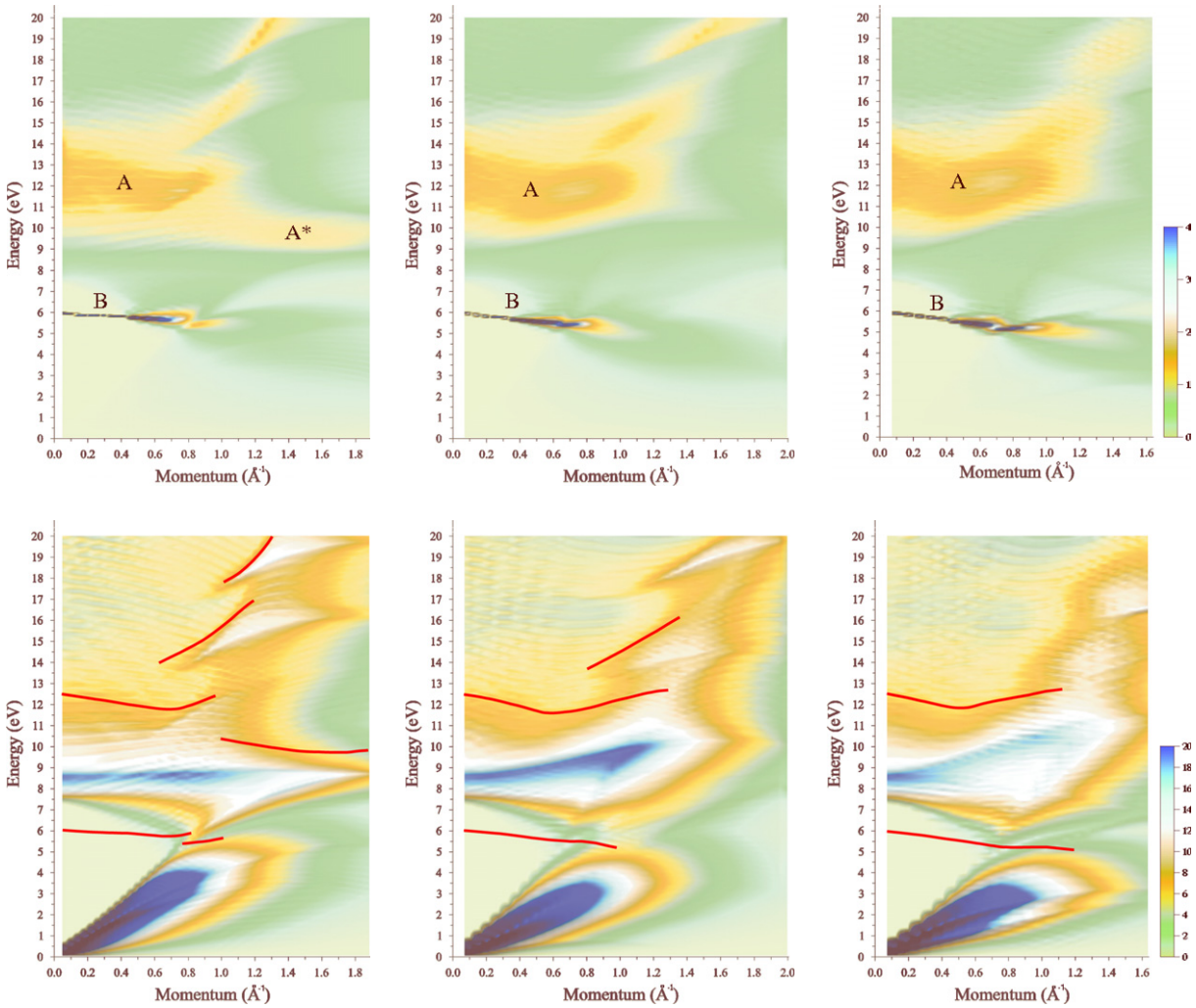

Figure 12. Top line: energy-loss spectra, $-\mathrm{Im}[\epsilon^{-1}]$, of fcc-Li at $P = 40$ GPa along the three symmetry directions: [100] (left panel), [110] (center panel), and [111] (right panel). CLFE and exchange-correlations are included. Bottom panel: damping function, $\omega \cdot \mathrm{Im}[\epsilon]$ of fcc-Li at $P = 40$ GPa along the same directions. Plasmon dispersions from the upper panels are plotted by solid red lines. Color codes are explained in the bottom right part of each panel of the figure. A clear absorption power redistribution from the free-electron-like plasmon 'A' to the undamped plasmon 'B' can be observed.

4. Conclusions

To summarize, in this paper, we have investigated the dielectric response of bulk lithium for a wide range of pressures from equilibrium up to 40 GPa. Energy-loss spectra, damping function, and plasmon dispersions and lifetimes are analyzed in detail. In addition, the role of band structure effects versus CLFE and exchange-correlation is investigated.

At equilibrium, besides the conventional free-electron-like plasmon, another kind of collective charge excitation emerges, which has been associated with a ZBCS mainly composed by inter-band transitions between occupied p-like and unoccupied s-like states around the

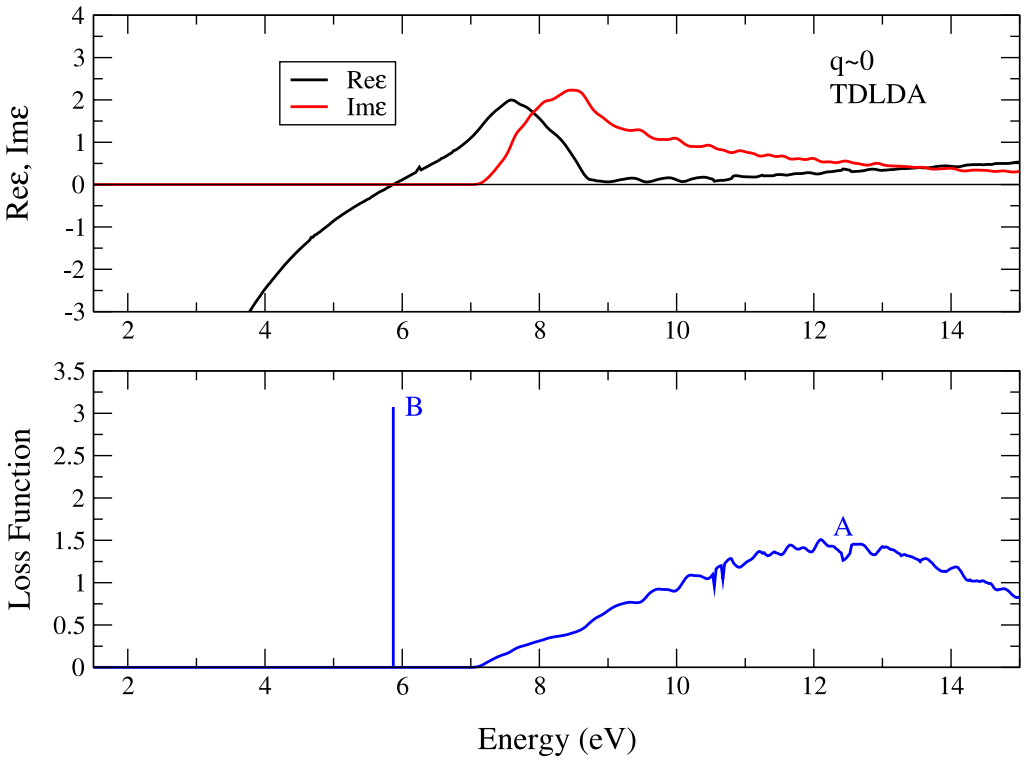

Figure 13. Top panel: low-momentum dielectric function of fcc-Li at $P = 40$ GPa. Re[ϵ] and Im[ϵ] are plotted by black and red lines, respectively. Bottom panel: corresponding energy-loss function with CLFE included. It is remarkable that at $\omega = 5.84$ eV the dielectric function vanishes, $\epsilon = 0$, which produces a δ-function-like peak in the energy-loss function at the same energy.

N point. In spite of this feature having been previously reported to arise only for high values of the momentum transfer along the [110]-direction, our calculations, based on the use of a denser sampling of the BZ, reveal that this ZBCS is also present at small but finite $|\mathbf{q}|$ and along the three directions considered. It is the special shape of the e–h excitation spectra along [110] which leads to the existence of the ZBCS at higher momenta along this direction, as it does not get scattered by any one-particle excitations. Both RPA and TDLDA approximations give similar results at small momentum transfers, with and without inclusion of the CLFE. Nevertheless, the CLFE become more influential when higher momentum transfers are considered, its effect being just quantitative but not qualitative.

Although the electronic band structure of bcc-Li is very free-electron-like, the two almost flat dispersions of the two lowest energy bands around the N point induce the appearance of the ZBCS. As we know, when increasing pressure the electrons strongly localize, which is reflected in an anisotropic flattening of bands. Therefore, we might expect the band structure effect to be even more influential in the electronic properties of fcc-Li at pressures ranging between 10 and 40 GPa. At 10 GPa we find again two different collective charge excitations. One of them, which is determined by the average valence electronic density, is very similar, when low momentum transfers are considered, to the conventional free-electron-like plasmon observed earlier for bcc-Li. However, in the higher momentum region (and specially along ΓX, where e–h excitations

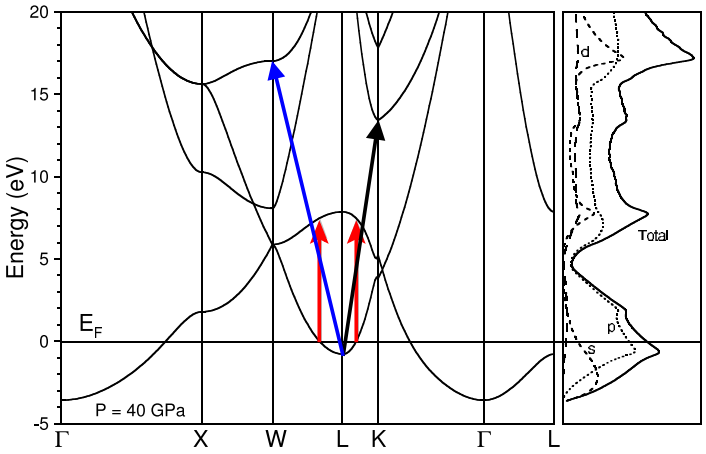

Figure 14. Energy band structure along some symmetry directions of the BZ (left panel) and DOS (right part) of fcc-Li at $P = 40$ GPa. The partial contributions to the total DOS from states of s, p, and d symmetries are denoted by corresponding symbols. The thresholds for the L–L, L–W, and L–K inter-band transitions are represented with red, blue and black arrows, respectively.

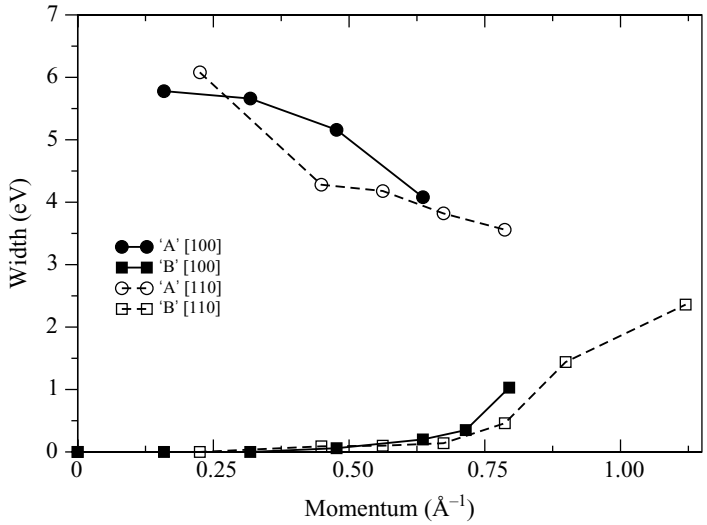

Figure 15. Plasmon width for fcc-Li at $P = 40$ GPa. Full (open) circles with a solid (dashed) line represent 'A' width along the [100] ([110])-direction. On the other hand, full (open) squares with a solid (dashed) line represent 'B' width along the [100] ([110])-direction.

reach the inter-band L–L transitions and rapidly decrease Im[ϵ]), the pressure enhanced band structure effects lead to a complex structure of the plasmon, which suffers several unfoldings due to different inter-band electronic excitations. More interestingly, another remarkable different feature arises at 10 GPa. At $|\mathbf{q}| = 0$, both real and imaginary parts of the dielectric function vanish, fulfilling the ideal condition for the existence of an undamped plasmon. This novel feature cannot decay via any intrinsic simple electronic scattering mechanism and, thus, leads

to the presence of a δ-peak in the energy-loss spectrum. Pressure drops electronic states near the L point below the Fermi energy and the presence of almost flat regions in both the occupied (mainly of p-symmetry) and unoccupied (mainly of s-symmetry) states around the L point leads to a step increase in $\mathrm{Im}[\epsilon]$ at 5.1 eV, which make both $\mathrm{Re}[\epsilon] = \mathrm{Im}[\epsilon] = 0$ at 4.7 eV. When low momentum dispersion is considered, it also remains undamped in any direction due precisely to the presence of these flat regions.

It is noteworthy that the ZBCS appearing in bcc-Li at equilibrium constitutes a predecessor of this undamped plasmon in fcc. At $P = 0$ GPa, we needed a finite $|\mathbf{q}|$ in order to excite the ZBCS because the N point was not occupied. However, if we consider bcc-Li at 10 GPa, the commented pressure-induced flattening of bands drops electronic states near the N point below the Fermi energy, which increases the number of possible N–N inter-band excitations (similarly to the case of fcc-Li with L–L optical transitions) with energy 5.5 eV. This enhances the ZBCS, becoming undamped and exhibiting a δ-peak in its energy-loss spectrum. Finally, if we further increase the pressure, at $P = 40$ GPa close to the fcc $\rightarrow hR1$ phase transition, we can observe that both the energy gap at the L point and the valence electron density increase. As a consequence, more energy is required in order to excite the optical inter-band transitions, which leads to a blueshift of the δ-peak in $\mathrm{Im}[\epsilon]$, and the energy of the conventional free-electron-like plasmon is also shifted. In addition, a clear absorption power redistribution from the free-electron-like plasmon to the undamped collective charge excitation is observed, as the pressure-induced flattening of bands produces an e–h excitation spectrum in such a manner that the undamped plasmon can extend to higher momentum transfers without being coupled to any one-particle excitations.

Finally, we hope that this work might stimulate experimentalists in order to check the existence of the ZBCS along the three directions considered for bcc-Li at equilibrium. Even more, now that inelastic x-ray scattering has made possible the measurement of plasmon dispersions under pressure [34], all the features presented for fcc-Li under pressure can, in principle, be experimentally tested.

Acknowledgment

We acknowledge partial support from the University of the Basque Country, the Basque Unibertsitate eta Ikerketa Saila, the Spanish Ministerio de Ciencia y Tecnología and the EC 6th framework Network of Excellence NANOQUANTA (NMP4-CT-2004-500198).

References

[1] Gibbons P C, Schnatterly S E, Ritsko J J and Fields J R 1976 *Phys. Rev.* B **13** 2451
[2] Schülke W, Nagasawa H, Mouikis S and Lanzki P 1986 *Phys. Rev.* B **33** 6744
[3] Schülke W, Nagasawa H and Mouikis S 1984 *Phys. Rev. Lett.* **52** 2065
[4] Hill J P, Kao C-C, Caliebe W A C, Gibbs D and Hastings J B 1996 *Phys. Rev. Lett.* **77** 3665
[5] Foo E-Ni and Hopfield J J 1968 *Phys. Rev.* **173** 635
[6] Karlsson K and Aryasetiawan F 1995 *Phys. Rev.* B **52** 4823
[7] Jin Y G and Ghang K J 1999 *Phys. Rev.* B **59** 14841
[8] Neaton J B and Ashcroft N W 1999 *Nature* **400** 141
[9] Bergara A, Neaton J B and Ashcroft N W 2000 *Phys. Rev.* B **62** 8494
[10] Hanfland M, Syassen K, Christensen N E and Novikov D L 2000 *Nature* **408** 174

[11] Rodriguez-Prieto A and Bergara A 2005 *Phys. Rev.* B **72** 125406
[12] Rodriguez-Prieto A, Bergara A, Silkin V M and Echenique P M 2006 *Phys. Rev.* B **74** 172104
[13] Rodriguez-Prieto A and Bergara A 2006 *High Press. Res.* **26** 461
[14] Rodriguez-Prieto A, Silkin V M and Bergara A 2007 *J. Phys. Soc. Japan* **76** 21
[15] Christensen N E and Novikov D L 2001 *Phys. Rev. Lett.* **86** 1861
[16] Tse J S, Ma Y and Tutuncu H M 2005 *J. Phys.: Condens. Matter* **17** S911
[17] Profeta G, Franchini C, Lathiotakis N N, Floris A, Sanna A, Marques M A L, Luders M, Massidda S, Gross E K U and Continenza A 2006 *Phys. Rev. Lett.* **96** 047007
[18] Kasinathan D, Kunes J, Lazicki A, Rosner H, Yoo C S, Scalettar R T and Pickett W E 2006 *Phys. Rev. Lett.* **96** 047004
[19] Christensen N E and Novikov D L 2006 *Phys. Rev.* B **73** 224508
[20] Tuoriniemi J, Juntunen-Nurmilaukas K, Uusvuori J, Pentti E, Salmela A and Sebedash A 2007 *Nature* **447** 187
[21] Shimizu K, Ishikawa H, Takao D, Yagi T and Amaya K 2002 *Nature* **419** 597
[22] Struzhkin V V, Eremets M I, Gan W, Mao H K and Hemley R J 2002 *Science* **298** 1213
[23] Deemyad S and Schilling J S 2003 *Phys. Rev. Lett.* **91** 167001
[24] Ashcroft N W 2002 *Nature* **419** 569
[25] Schilling J S 2006 *Treatise on High Temperature Superconductivity* (Hamburg: Springer)
[26] Silkin V M, Rodriguez-Prieto A, Bergara A, Chulkov E V and Echenique P M 2007 *Phys. Rev.* B **75** 172102
[27] Runge E and Gross E K U 1984 *Phys. Rev. Lett.* **52** 997
[28] Petersilka M, Gossmann U J and Gross E K U 1996 *Phys. Rev. Lett.* **76** 1212
[29] Perdew J P and Zunger A 1981 *Phys. Rev.* B **23** 5048
[30] Troullier N and Martins J L 1991 *Phys. Rev.* B **43** 1993
[31] Aryasetiawan F and Gunnarsson O 1994 *Phys. Rev.* B **49** 16214
[32] Miyake T and Aryasetiawan F 2000 *Phys. Rev.* B **61** 7172
[33] Kloos T 1973 *Z. Phys.* **265** 225
[34] Loa I *et al Proc. Joint 20th AIRAPT–43rd EHPRG Conf.* (unpublished)